CO-PROX on MnO_2 catalysts: DFT-based microkinetic and experimental macrokinetic approaches

L. Gueci[a], F. Arena[b,*], S. Todaro[c], G. Bonura[c], A. Cajumi[b], M. Bertini[a], F. Ferrante[a,*], C. Nania[a], D. Duca[a]

[a] *Dipartimento di Fisica e Chimica "E. Segrè" - Università degli Studi di Palermo, Viale delle Scienze Ed. 17, I-90128 Palermo, Italy*
[b] *Dipartimento di Ingegneria, Università di Messina, C.da Di Dio 1, 98765 Messina, Italy.*
[c] *Istituto CNR-ITAE "Nicola Giordano", Salita S. Lucia 39, I-98126 S. Lucia, Messina, Italy.*

Abstract

A microkinetic analysis in terms of DFT-calculated temperature-dependent Gibbs free energies was performed for the oxidation reactions of CO and H_2 on a model Mn_4O_8 cluster. Apparent activation energies data predict a peculiar CO preferential oxidation pattern of Mn(IV) sites in presence of hydrogen (PROX) substantiated by the unprecedented PROX behavior of a nanocomposite $MnCeO_x$ catalyst in the range of 353-423K under both ideal and real process conditions. Micro- and macrokinetic data on the "model" cluster and "real" catalyst are discussed.

Keywords: H_2 Purification, Manganese Oxide, Computational Catalysis, TPR

---

1. Introduction

The oxidation reactions of carbon monoxide and hydrogen are amongst the most popular model reactions in catalysis routinely employed for catalyst screening, characterization, and mechanistic studies as well. Nowadays, these reactions have also gained a great practical interest due to the potential of H_2 oxidation in Fuel Cells for clean energy production, and the environmental threat of CO being a highly toxic compound also

---

*Corresponding authors

Email addresses: `laura.gueci@unipa.it` (L. Gueci), `francesco.arena@unime.it` (F. Arena), `serena.todaro@itae.cnr.it` (S. Todaro), `giuseppe.bonura@itae.cnr.it` (G. Bonura), `alessandro.cajumi@studenti.unime.it` (A. Cajumi), `marco.bertini@unipa.it` (M. Bertini), `francesco.ferrante@unipa.it` (F. Ferrante), `chiara.nania@unipa.it` (C. Nania), `dario.duca@unipa.it` (D. Duca)

Preprint submitted to Catalysis Today *February 28, 2024*

source of secondary pollution issues (i.e., formation of ground-level ozone). Moreover, the preferential oxidation of CO (PROX) is being explored as a viable alternative to methanation or adsorption (PSA) for cleaning up H_2-feeds in catalytic technologies like Hydrogenation, Ammonia Synthesis, and Fuel Cells [1, 2].

Noble-metal catalysts such as Pt, Rh, Ir, and Au are extensively studied for their PROX performance, and innovative design strategies, such as single atom catalyst (SAC) formulations, have been devised to improve their activity pattern [2–6]. In fact, SAC's exploit the reactivity of suitable carriers and/or promoters to trigger dual-site reaction paths overcoming the limitations of competitive adsorption seen in conventional systems. Meanwhile, economics and sustainability issues drive a great attention on transition-metal (TM) catalyst compositions (Cu, Co, Mn, Ce, etc.) for their enhanced CO oxidation activity [2, 6–8] and a PROX performance comparing to noble metals [3, 7–15]. Thus, many studies have focused on understanding the CO oxidation mechanisms and fundamental clues of the PROX behavior for TM-based catalysts, like CuO_x [9, 10, 14], CoO_x [13, 15–18], and MnO_x systems [10–12]. In this respect, it has been found that the PROX functionality of the $CuCeO_x$ catalyst depends on metal Cu sites that are unstable under complete CO conversion conditions [14], while the PROX behavior of Co catalysts is very sensitive to the oxidation state of Co sites due to the blocking effects of carbonate species [13, 16, 17]. Moreover, DFT and kinetic studies using isotopically labeled oxygen were adopted to explore the mechanistic clues of the PROX functionality of $CoMnO_x$ catalysts [17, 18], while we recently carried out a comparative DFT study of the oxidation functionality of Mn(IV) sites toward CO and H_2, predicting and further documenting an appealing PROX behavior of MnO_2 catalysts for PEMFC's technology [10]. At variance, a crucial role of hydroxyl groups was raised to explain the PROX behavior of $\varepsilon-MnO_2$ systems [12].

Therefore, aiming at a deeper understanding of the kinetic issues and molecular aspects of the peculiar PROX functionality of the MnO_2 catalyst, this study presents a microkinetic analysis of the DFT mechanisms of CO and H_2 oxidation on a model Mn_4O_8 cluster, in terms of Gibbs energy of the various elementary reaction steps in a wide range of temperature. Using a new approach named Simplified Christiansen Method (SCM), specifically designed to manage kinetic analyses by quantum chemical descriptors [19], microkinetic data describe the CO and H_2 oxidation pattern shedding light into the mechanistic issues determining PROX functionality of "real" MnO_2 catalysts. The Mn_4O_8 cluster here employed was considered as representative of the nanoformations occurring in the high dispersed MnO_2 phase present in MnO_x catalysts [20–22]; its geometrical and electronic properties were reported in previous works [10, 23, 24]. As a matter of fact, just considering only very recent works, the long-time studied sub-nanometer manganese oxide clusters have been the object of joint experimental-computational investigations for their potential catalytic activity in processes regarding biomass valorization [25, 26], water splitting reaction [27], hydrogen oxidation [28] and pollutant degradation [29].

2. Experimental

2.1. Computational Details

Reported density functional theory data are based on calculations obtained by using the M06L exchange-correlation functional [30] joined with the correlation consistent polarized valence double zeta, cc-pvdz, basis set for light atoms [31] and the Relativistic Small Core Stuttgart ′97 basis set equipped with effective core potentials for manganese [32]. All calculations were done by using the Gaussian 09 program [33]. Christiansen analysis was performed by means of a home-made code, which, in its general conception, is able to find all the possible reaction paths between reactants and products when reaction energies and barriers of all elementary processes are provided and to analyze them according to the Simplified Christiansen Method [19] to give global reaction rates. The free energies values of all the intermediates involved in the various reaction steps were obtained considering the quasi-harmonic correction to entropy proposed by Grimme [34], with a frequency cutoff of 100 cm^{-1}, using the Goodvibes code [35].

2.2. Materials and Methods

The nanocomposite $MnCeO_x$ catalyst (M5C1) was prepared via the redox-precipitation synthesis technique [10, 36]. The chemical composition was probed by X-Ray Fluorescence (XRF) analysis while surface area, pore volume and average pore diameter data were obtained from the N_2 adsorption-desorption isotherm (77K) elaborated by the BET and BJH methods, respectively. Temperature Programmed Reduction analyses in the range of 293-773K were performed with a heating rate of 12 K min^{-1} using a quartz reactor containing 20 mg of catalyst, fed with either 5% H_2/Ar (H_2-TPR) or 5% CO/He (CO-TPR) carriers (F, 60 *stp* mL min^{-1}).

The CO and H_2 oxidation activity of the M5C1 catalyst was probed by temperature programmed reaction tests in the range of 293-533 K at heating rate of 2 K min^{-1} using a QMS as analytical tool [10]. The testing was carried out using 20 mg of catalyst diluted with granular SiC, feeding reaction mixtures containing CO or H_2 (2.5%) and O_2 (2.5%) in He (95%) at the rate of 60 *stp* mL min^{-1} (GHSV, $1.8{\cdot}10^5$ h^{-1}). The PROX pattern under kinetic regime was probed in the same apparatus (GHSV, $1.8{\cdot}10^5$ h^{-1}), feeding a stream containing 1% CO, 1% O_2 and 60% H_2 (He, rest) that was analyzed on line by the QMS. Integral conversion PROX tests (GHSV, 720 h^{-1}) were performed in isothermal regime (T, 353-423K) using a CO (1%), O_2 (1%), H_2 (85%) and N_2 (13%) (F, 60 stp mL min^{-1}) mixture cyclically analyzed by a GC equipped with dual-column system and TCD for detection of O_2, N_2, CO and CO_2 [10].

3. Results and Discussion

3.1. DFT Mechanisms and Christiansen Analysis of Energy Data

The oxidative functionality of Mn(IV) sites toward CO and H_2 has been assessed by DFT calculations on a Mn_4O_8 model cluster (in the following also indicated as the oxygenated fragment), as reported in our previous work [10]. The whole DFT catalytic cycle, illustrated in Figure 1, was characterized in terms of atomistically-resolved elementary steps and is the result of the exploration of a large number of possible pathways starting from the available adsorption sites for CO and H_2 on Mn_4O_8. According to the proposed mechanism for carbon monoxide oxidation, the first CO molecule is transformed to CO_2 by means of atomic oxygen extracted from the cluster, with the formation of the under-oxygenated Mn_4O_7 species (**4**). This can promptly adsorb one O_2 molecule, forming the hyper-oxygenated fragment Mn_4O_9 (**5**), whose excess oxygen atom is ready to easily convert another CO molecule, so that the starting model cluster is restored. The energetic details of the catalytic cycle of Figure 1 can be preliminarily discussed in terms of electronic energies including vibrational zero-point contribution, corresponding to Gibbs free energies at 0 K. CO adsorption on Mn_4O_8 occurs with the release of only 25 kJ mol^{-1}, and a energy barrier equal to 52 kJ mol^{-1} must be overcome for the conversion to the $Mn_4O_7{-}CO_2$ intermediate. The desorption of carbon dioxide from Mn_4O_7 would require ca. 60 kJ mol^{-1}, so that the global energy release for the first CO molecule oxidation process sum up to 142 kJ mol^{-1}. The oxidation of the second CO molecule, on the other hand, starts from the Mn_4O_9 species, and involves the release of 40 kJ mol^{-1} for CO adsorption and an energy barrier of 45 kJ mol^{-1}; considering that the final products are Mn_4O_8 and CO_2, a reaction energy difference of 387 kJ mol^{-1} was evaluated [10].

Regarding H_2 oxidation, our investigation ruled out the possibility that the hydrogen molecule could give rise to sensible interactions with the Mn_4O_8 cluster, but showed that H_2 can be adsorbed, with the release of 21 kJ mol^{-1}, on the hyper-oxygenated site of Mn_4O_9. This species forms as intermediate in the CO oxidation reaction, but in order to make the H_2 oxidation independent from the presence of carbon monoxide, its formation could be hypothesized directly from Mn_4O_8, by surface and near-surface oxygen spillover phenomena. On Mn_4O_9, H_2 breaks as a result of the overcoming of a energy barrier as high as 107 kJ mol^{-1}. After some rearrangments, which involve the presence of intermediates where the H atoms are first separately located on Mn and O centers (**9**, **10**, which interconverts the one to the other with an energy barrier of 47 kJ mol^{-1}), and then both on O (**11**, where incidentally the O−O present in Mn_4O_9 is broken and an energy barrier of 100 kJ mol^{-1} is present on the path), a further H-shift from oxygen to oxygen leads to (**12**), from which a water molecule can desorb, requiring 73 kJ mol^{-1} of energy. The whole reaction energy release accompanying the conversion of $Mn_4O_9 + H_2$ to $Mn_4O_8 + H_2O$ is equal to 275 kJ mol^{-1} [10].

In order to convert the DFT energy values into figures that can be copared with the experimental data, the microkinetic simplified Christiansen method was employed. SCM aims to determine the overall rate s of a given reaction path by solving the system of equation

$$\frac{1}{s}\begin{vmatrix} \bar{w}_1 & -w_{-1} & 0 & \cdots & 0 \\ 0 & w_2 & w_{-2} & \cdots & 0 \\ 0 & 0 & w_3 & \cdots & 0 \\ \vdots & \vdots & \vdots & \ddots & \vdots \\ w_{-n} & 0 & 0 & \cdots & w_n \end{vmatrix} \begin{vmatrix} \theta_1 \\ \theta_2 \\ \theta_3 \\ \vdots \\ \theta_n \end{vmatrix} = \begin{vmatrix} 1 \\ 1 \\ 1 \\ \vdots \\ 1 \end{vmatrix} \tag{1}$$

which is constructed by considering the direct and reverse kinetic constants (determined by the corresponding DFT calculated energy barrier, E_b, values)

$$w_j = \frac{\mathrm{kT}}{\mathrm{h}} \mathrm{e}^{-\mathrm{E}_b(j \to j+1)/\mathrm{RT}} \tag{2}$$

$$w_{-j} = \frac{\mathrm{kT}}{\mathrm{h}} \mathrm{e}^{-\mathrm{E}_b(j+1 \to j)/\mathrm{RT}} \tag{3}$$

of a sequence of elementary steps in imposed quasi-stationary condition, with the species 1 and $n + 1$ corresponding to the isolated gas phase reactants and products, respectively. The θ_i represent the fraction of sites occupied by the species i, being, in particular, θ_1 associated to the empty site fraction. Besides, SCM can be fruitfully used to help discriminating between various competitive pathways in complex reaction networks [37, 38], where the simple analysis of energy barriers and reaction energies cannot be trusted due to the complexity and length of all possible interlaced pathways.

The microkinetic analysis here reported is performed on the published DFT data for reaction energies and barriers corresponding to two reaction pathways. In particular, the considered processes are: a) carbon monoxide oxidation going from species **1** to **7**, followed by catalyst restoration, b) the H_2 route starting from the hyper-oxygenated cluster (species **5**), obtained from **1** by assuming an oxygen spillover process. The SCM analysis was performed in terms of Gibbs free energies as a function of the temperature (ranging from 373 to 523 K, at P = 1 bar). Considering the continuous flow conditions, it is assumed that product molecules desorbing from the cluster cannot be re-adsorbed, while when adsorption is endoergonic (as in the CO and H_2 cases, whose desorption is entropy-driven), the possibility of a reactant leaving the system was considered. Once the free energies variation along all paths (reported in Table 1) were outlined and SCM performed to obtain the reaction rates (see Table 2) at a given temperature [19, 24], the apparent activation energies for CO and H_2 oxydation processes were evaluated through Arrhenius plots. It resulted that the calculated apparent activation energy, E_a^{clc} value, for CO oxidation on the Mn_4O_8 model catalyst is equal to 24 kJ mol^{-1}, while the one calculated for H_2 conversion to water is evaluated as 96 kJ mol^{-1}, witnessing a remarkable preferential oxidation of carbon monoxide with respect to molecular hydrogen.

[Figure 1 about here.]

[Table 1 about here.]

[Table 2 about here.]

3.2. Reactivity of the "real" MnO_2 catalyst toward CO and H_2 in absence of O_2: the reduction pattern.

The experimental study aimed at ascertaining the practical feasibility of computational findings started with the design of a material with prevalent exposure of "isolated" Mn(IV) sites representative of the model Mn_4O_8 cluster. Thus, exploiting the effectiveness of the redox-precipitation synthesis route in promoting the oxide dispersion, a nanocomposite $MnCeO_x$ system including small amount of the ceria promoter (Ce_{at}/Mn_{at}, 1/5) was synthesized as the experimental counterpart of the model cluster (M5C1) [10, 36]. Due to the structural effects of ceria [10, 36, 39], it features a typical mesoporous texture with surface area, pore volume and average pore diameter of 159 m^2/g, 0.55 cm^3/g and 30 nm, respectively. Moreover, according to a surface Mn/Ce atomic ratio (5.1) larger than bulk one (4.75), the XPS analysis signals a surface Mn enrichment, mostly in the +4 oxidation state (Table 3), and with an average oxidation number (AON) of +3.67 [10, 36]. In addition, a featureless XRD pattern discovers a very poor crystalline arrangement substantiated by the lack of F_{2g} Raman signal of cerianite (≈ 460 cm^{-1}) in the Ramam spectrum of the synthesized material. These structural data denote an extensive incorporation of Ce ions into the MnO_x structure hindering, in turn, the thermally-driven nucleation of ceria clusters and the $\delta - \to \alpha$–MnO_2 phase transition, as indicated by smoothed Raman signals at 502, 573 and 650 cm^{-1} and a bulk K/Mn atomic ratio of 0.13 typical of the layered birnessite phase (Table 3) [10, 12, 36, 39].

Large surface availability and strong redox activity of Mn(IV) atoms shape in turn the reduction pattern of the M5C1 catalyst that was comparatively probed by CO-TPR and H_2-TPR measurements shown in 2. Like the bare MnO_2 system, indeed, both patterns display two resolved peaks in the range of 293-723K accounting for comparable extents of CO and H_2 consumption (CO/Mn-H_2/Mn, 0.85-0.87) mirroring the above AON [10, 36]. An amplitude ratio of ca. 2:1 signals a stepwise reduction of MnO_2 nanodomains to Mn_3O_4 and MnO respectively, although a three-step process coming across the intermediate Mn_2O_3 species cannot be disregarded [12, 40, 41]. Apart from a shift to lower temperature of the peak maxima due to higher MnO_2 dispersion, in fact, the similar TPR patterns of bulk MnO_2 and M5C1 catalysts denote a negligible, if any, influence of ceria on the electronic properties of surface MnO_2 sites [10, 21, 22, 36]

[Table 3 about here.]

Despite such similar features, however, a considerable downward shift of the first peak (≈85K) signals a much easier reduction of Mn(IV) sites by CO, while the ensuing reduction of the Mn_3O_4 phase is almost insensitive to the reductant (Fig. 2) [10, 36]. Thus, to get insights into the energy barriers for reduction of Mn(IV) sites the uphill branch of the first peaks was elaborated into Arrhenius plots considering a pseudo-first order kinetic equation

$$\text{reduction rate} = k_{\text{app}} \cdot p_X^a \cdot N_{\text{site/g}} \cdot (1 - \alpha/0.67) \tag{4}$$

where α is the reduction degree, (*i.e.*, the fraction of reduced Mn(IV) sites given by the integral of TPR curves between 293K and T) divided by the number of O-atoms extracted from each MnO_2 site in the first reduction step (*i.e.* $MnO_2 \longrightarrow MnO_{1.33}$), $N_{\text{site/g}}$ are the moles of Mn(IV) atoms per gram of catalyst, p_X is the pressure of the reductant and a is the relative reaction order. The logarithmic form of eq. (4)

$$\ln \frac{\text{reduction rate}}{1 - \alpha/0.67} = \ln k_{\text{app}} + a \ln(p_X) + \ln(N_{\text{site/g}}) \tag{5}$$

shows that the left-term vs. the reciprocal of temperature represents the Arrhenius plot of the rate constant, since the last two terms are constant because of differential CO and H_2 consumption (<10%) throughout the measurements. In both cases such an elaboration gives reliable straight-line relationships which account for apparent activation energy (E_{red}) values of 44 ± 1 and 68 ± 1 kJ mol^{-1} for the reduction of Mn(IV) sites by CO and H_2, respectively (Fig. 2C). Matching at a molecular level the increasing reactivity of the Mn(IV)-O bond with temperature (v. *supra*), these figures reflect growing populations of Mn(IV) sites (i.e., α) reactive toward CO and H_2 on the "real" catalyst. This issue is further discussed in the final paragraph.

[Figure 2 about here.]

3.3. Activity pattern of the "real" MnO_2 catalyst toward CO and H_2 in presence of O_2.

Since O-vacancies act as O_2 adsorption centers throughout the reaction cycle, it is lilkely that the considerable E_{red} gap (20-25 kJ mol^{-1}) would affect the CO and H_2 oxidation activity pattern of the M5C1 catalyst (Fig. 3). In fact, activity data under kinetic regime (GHSV, 180,000 h^{-1}) document a much stronger CO oxidation activity with conversion values rising from 0 to 100% in the range of 293-533 K, while the H_2 oxidation starts only at $T \geq 393K$ reaching a maximum conversion of 15% at 533K (Figure 3A). Assuming 1^{st}-order kinetics, consistent with the sigmoidal CO conversion trend, conversion data (e.g., $\ln[-\ln(1-X)] = \ln[k] + \ln[\tau]$) in the ranges of 323-523K and 433-523K depict reliable Arrhenius plots (Figure 3B), indicating E_{rx} values of 49±3 and 69±3 kJ mol^{-1} for the CO and H_2 oxidation, respectively. Matching the relative E_{red} data, these figures establish a close relationship between reducibility and oxidation activity of MnO_2 catalysts suggesting that the abstraction of catalyst O-atoms is the rate determining step (r.d.s.) of both CO and H_2 oxidation. [12, 40–48]. This finding matches previous evidences of the key-role of lattice oxygen mobility on the PROX behavior of bare and Cu-doped MnO_x systems [46], although recent studies related a high CO oxidation performance [47] and the PROX activity pattern of ε-MnO_2 materials to surface defects and hydroxyl groups prompting a favorable hydroxycarbonate-intermediate reaction path [12, 48]. However, even if the formation of several carbonate intermediates at the surface of MnO_2 catalysts testifies a strong chemical affinity of Mn(IV) sites toward CO, the nature of "active" oxygen species remains a controversial issue [10, 12, 36, 41, 42, 44–47, 49, 50]. Despite fractional orders on CO and O_2 are related to L-H paths involving adsorbed CO and O_2 at T<423K [12, 44–48, 51, 52], experimental evidences reveal the occurrence of a typical redox mechanism.

[Figure 3 about here.]

Thus, to rule out any role of adsorbed O_2 species on the activity pattern of the M5C1 catalyst in the studied range of temperature, a H_2-TPR analysis after an in situ treatment at 673 K in O_2 flow has been performed (Fig. 4).

[Figure 4 about here.]

Favoring the removal of adsorbed species (i.e., H_2O, CO_2, etc.), the pretreatment prompts O_2 adsorption onto O-vacancies and defects resulting in larger H_2 consumption with respect to the untreated counterpart [10], as observed for a reference $MnCeO_x$ catalyst (Mn_{at}/Ce_{at}, 1) showing after pretreatment an additional peak centered at 403 K, previously ascribed to O_2 species adsorbed onto electron-donor Mn(II)-CeO_2 solid-solution centers (Fig. 4) [36]. By contrast, an almost unchanging profile confirms that the functionality of Mn(IV) surface sites rules the reactivity of the M5C1 catalyst according to the following simplified mechanisms (see Scheme 1)

- (step a) CO adsorbs on Mn(IV) sites (σO) producing a carbonate-intermediate (step a) that decomposes forming CO_2 and an O-vacancy (σ) (step b). Afterward, the interaction of O_2 with the reduced site (step c) leads to the formation of adsorbed oxygen species (σO_2) that easily interact with another CO molecule (step d) giving the second carbonate-intermediate that decomposes into the second CO_2 molecule restoring the pristine Mn(IV) site (step e) [10, 44, 45]. Notably, the possible contribution of surface hydroxyls is not considered for the sake of simplicity of the above reaction mechanism [12, 47] and in consideration of the general negative effect of wet reaction streams on the activity pattern of the M5C1 catalyst [10, 36].
- At variance, the interaction of H_2 with Mn(IV) sites with comes across a preliminary formation of diatomic oxygen species that, in absence of O_2 (*i.e.*, TPR), should be the result of O-spillover process (step a′) [10]. This was previously argued in the light of the O_2 desorption pattern, and it is further supported by a recent study stressing a crucial role of O-vacancies that, favoring the mobility of oxygen atoms and molecules at the surface of the $\beta-MnO_2$ catalyst, drive the H_2 oxidation cycle at $T \geq 373K$ [53]. In fact, Yang *et al.* investigated the evolution of reactive oxygen species (ROS) in the range of 288-328 K on different crystal planes of birnessite coming to the conclusion that ROS can be generated and transformed changing temperature owing to the promoting effect of O-vacancies [50]. Adsorbed oxygen species prompt then H_2 adsorption, leading the formation of water and replenishment of a Mn(IV) site (steps c′-e′). The residual reduced site acts as an O_2 adsorption center running the catalytic cycle in presence of O_2 (step b′) [10].

[Scheme 1 about here.]

Thus, after such preliminary confirmations of computational findings, PROX tests (i.e., p_{CO}, 1 kPa; p_{O_2}, 1 kPa; p_{H_2}, 60-85 kPa) under both differential (Fig. 5A) and integral (Fig. 5V) conversion conditions have been performed.

[Figure 5 about here.]

Despite an overwhelming H_2 concentration (H_2/CO, 60), at the same GHSV of previous tests the activity pattern of the M5C1 catalyst looks like that recorded for the two substrates separately (Figure 3A). In fact, nearly unchanged CO conversion values and no H_2 oxidation activity are observed in the range of 293-393K (Fig. 5A), whereas, at T>393 K the incipient H_2 oxidation lowers the O_2 concentration depressing CO conversion levels. Since the CO oxidation cycle evolves through the formation of diatomic oxygen species, this finding proves that the activation energy gap of the reduction processes is the key-factor shaping the PROX functionality of the M5C1 catalyst. Indeed, at integral conversion conditions (GHSV, 720 h^{-1}) the M5C1 catalyst ensures a full CO conversion (96-100%) and CO_2 selectivity values decreasing from 100 to 60% in the range of 353-423K (Fig. 5B), corresponding to a hydrogen loss lower than 1%. Finally, good stability and PROX behavior also in a simulated WGS stream substantiate the potential of the studied catalyst for PEMFC's technology [10].

3.4. Refining DFT data

The data reported and analyzed above indicate that the experimental values of the apparent activation energy for the investigated oxidation reactions are 45 and 68 kJ mol^{-1} (Fig. 2C), respectively, while the values estimated by the computational investigation are, correspondingly, 24 and 96 kJ mol^{-1}. Therefore, the ratio between the values of the apparent activation energies of the CO and H_2 conversion processes are 0.67 and 0.25 according to the experimental and computational results, respectively. This discrepancy should not surprise, though. The DFT/SCM evaluation of the surface processes actually refers to transformations that occur on one isolated site, ideally identified as the reaction site. With this, it is not considered how many reaction sites actually exist with respect to the catalytic surface sites and how their numeric ratio varies, for example, with changing the temperature. This dependence indeed exists in the PROX here studied and it is attested by the trends, with the temperature, of the reduction degree, α, referred to the CO and H_2 processes and reported in Figures 2A,B.

Another aspect whose effects cannot be evaluated with the DFT/SCM approach is the competition of different processes taking place on different active sites/oxygen species. In fact, the DFT study shows that there are two different kinds of catalytic sites driving the CO oxidation, namely those on the fragments 1 and 5 of Figure 1. Moreover, fragment 5, already denoted as hyper-oxygenated, is originated by fragment 1 and is involved in the oxidation of H_2, too. Due to the temperature-dependent surface and near-surface spillover phenomena, the relative number of active sites changes as the temperature varies. Thus, it is conceivable that the effect of the competition for the hyper-oxygenated sites, common to the two oxidations, should depend on the temperature.

Summarizing the experimental and computational evidence by points:

- The DFT/SCM approach refers to one model site that evolves over time until equilibrium is reached [19]. The result of the corresponding simulation considers neither the nature and effective number of surface sites nor the competition that could occur between different species on the same site.
- Inferences based on DFT analysis are in agreement with a temperature-activated H_2 oxidation, also suggesting dedicated surface sites for this process. Interestingly, these results are coherent with the experimental findings.
- The oxidation of CO, referring to the DFT/SCM approach, takes place on two different sites, characterizing the oxygenated and hyper-oxygenated fragments on which the process seems to be slightly favoured. Computational findings confirm that the oxidation of H_2 conversely occurs just on the latter.
- The DFT values of ΔG reported in Table 1, related to the adsorption of H_2 and CO, show that the former should be favoured over the latter, irrespective of the temperature values, on the hyper-oxygenated fragments.
- The experimental α trends, for both CO and H_2, clearly show that the number of reaction sites increase with the temperature. The effect of the temperature on the reaction steps taking place on the hyper-oxygenated sites should be even more effective since the activation ΔG values for the processes occurring on these fragments are lower than the ones characterizing the remaining fragments involved in the whole mechanism.
- Given the last two previous points, with the temperature there must therefore be a

proportional increase i) in the oxidation of CO and ii) in the competitive behaviour of CO and H_2 for the same surface sites.

Interestingly, it is possible to make the computational and experimental behaviors of the apparent activation energy ratios each other more similar if it is admitted that the oxidation rate of CO, on the whole, takes an advantage over that of H_2 on the hyper-oxidate surface sites, as the temperature increases. In this way, in fact, the apparent activation energy of the CO oxidation would increase, while that of H_2 would decrease, both becoming more similar to the, singly corresponding, experimental findings.

It is possible to model this inference by fractionating a given DFT/SCM reference site into a quantity π, increasing with the temperature, referred to one process and, for simplicity, a quantity $(1 - \pi)$ referred to the other process. In passing, it is here stressed that this phenomenological model as a whole does not contrast with the items in the list above and on the contrary is especially consistent with the points of the list concerning the temperature dependence of the surface phenomena and, in particular, with the competition for the hyper-oxygenated sites of the two oxidation processes. The hypothesized model behavior is finally in agreement also with the Arrhenius trends, calculated and experimental, which have been determined for the oxidation of CO and H_2, showing, independently of the approach followed, a ratio between the values of the apparent activation energies of the CO and H_2 oxidation always less than 1.

Following the proposed modeling a phenomenological perspective, both the π descriptors above would evaluate the probability of occurrence at different temperatures of one or the other oxidation on the surface sites, in this way, normalizing the rate of a given catalytic transformation to the whole surface sites and to the competition of the two oxidations on the same ones. In fact, π and $(1 - \pi)$ define the probabilities of reaction for the reagents of the PROX averaging, for the single species, on the number of surface sites involved into a given process and on the properties of the different processes characterizing each species. For simplicity, we can think π:

$$\pi = \mathrm{e}^{-\beta/\mathrm{RT}} \tag{6}$$

as a multiplying term of the reaction rate, $\mathrm{s_{CO}}$, of the whole CO oxidation process:

$$\pi \cdot \mathrm{s_{CO}} \propto \mathrm{e}^{-\beta/\mathrm{RT}} \cdot \mathrm{e}^{-\mathrm{E}_a^{clc}/\mathrm{RT}} \tag{7}$$

where E_a^{clc} is the calculated apparent activation energy and $E_a^{exp} = E_a^{clc} + \beta$ the experimental one. The same could, of course, be done in order to correct the s_{H_2} rate, in this case, at variance, using the multiplying term $(1 - \pi)$.

Since hydrogen oxidation is a kinetically less significant parasitic process, it is preferable to refer in the first instance to the complementary CO oxidation. Due to this, it is clear that a simple choice for the β correction value is ca. 20 kJ mol^{-1}, which brings the calculated activation energy to the experimental value. For this value of β the correction of the activation energy in the oxidation process of H_2 amounts to ca. 2%. In any case, the calculated apparent activation energy of the H_2 oxidation is, however, rather insensitive to the parameter $(1 - \pi)$, for β values that have physical significance, with respect to the activation energy barrier of the CO oxydation. The ratio of the apparent activation energy values characterizing the two oxidations involved in the here modeled PROX, for $\beta = 20$ kJ mol^{-1}, increases to ca. 0.5.

These findings, although based on rather naive considerations, heuristically justify the just apparent lack of kinetic correlation between the two processes and the preference of hyper-oxygenated sites, *i.e.* those of the fragment 5, in both the processes. However, the CO oxidation is extremely favored on these. Therefore, it can finally be inferred that the presence of bulk-oxygen spillover, activated by the increasing of the temperature and not explicitly manageable in the frame of the DFT/SCM approach, is at the basis of the discrepancy between the calculated and experimental findings of the apparent activation energy in the PROX processes here analyzed.

3.5. Conclusions

The oxidation functionality of surface Mn(IV) atoms determines the typical PROX behavior of a nanacomposite $MnCeO_x$ catalyst. A significant activation energy gap promotes CO oxidation at 293 K hindering the H_2 oxidation below 393 K. Microkinetic analysis based on the application of the Simplified Christiansen method on reaction energetics calculated by Density Functional Theory shows satisfactory agreement with the empiric kinetic parameters. Microkinetic analysis also emphasizes the decisive role of changes in the oxidation state during the catalytic reaction at sites identified with units containing just MnO_x fragments, with ceria serving as support and dispersing element for active site. The alignment of experimental results with the proposed kinetic model has been also improved by introducing a descriptor governing the probability occurrence of the different catalytic oxidation cycles involved.

References

[1] H. Zhang, S. Fang, Y. Hu, Catal. Rev. 64 (2022) 491.532.

[2] H. Liu, D. Li, J. Guo, Y. Li, A. Liu, Y. Bai, D. He, Nano Res. 16 (2023) 4399–4410.

[3] P. Jing, B. Gong, K. Liu, J. Zhang, Catal. Sci. Tech. (2020) 919.

[4] Y. Chen, J. Liu, Int J. Hydr. En. 48 (2023) 24788–24808.

[5] Y. Pan, S. Hwang, X. Shen, J. Yang, J. Zeng, M. Wu, Z. Peng, ACS Catal. 8 (2018) 5777–5786.

[6] N. K. Soliman, J. Mater. Res. Technol. 8 (2019) 2395–2407.

[7] S. Dey, G. Dhal, D. Mohan, R. Prasad, Adv. Composite and Hybrid Mater. 2 (2019) 626–656.

[8] J. Meißner, L. Ahrens, J. Pasel, A. Achwedt, S. Wohlrab, J. Mayer, R. Peters, Sci. Rep. 13 (2023) 9345.

[9] R. Jokar, S. Alavi, M. Rezaei, E. Akbari, Int. J. Hydr. En. 48 (2022) 24833–24844.

[10] F. Arena, F. Ferrante, R. Di Chio, G. Bonura, F. Frusteri, L. Frusteri, A. Prestianni, S. Morandi, G. Martra, D. Duca, Appl. Catal. B 300 (2022) 120715.

[11] A. Davó-Quiñonero, E. Bailón-García, S. López-Rodríguez, J. Juan-Juan, D. Lozano-Castelló, M. García-Melchor, H. F. C., E. Pellegrin, C. Escudero, A. Bueno-López, ACS Catal. 10 (2020) 6532–6545.

[12] Z. Zhang, Y. Tian, W. Zhao, P. Wu, J. Zhang, L. Zheng, T. Ding, Catal. Today 355 (2021) 214–221.

[13] L. Zhong, T. Kropp, W. Baaziz, O. Ersen, D. Teschner, R. Schlögl, M. Mavrikakis, S. Zafeiratos, ACS Catal. 9 (2019) 8325–8336.

[14] Y. Bu, S. Er, J. Niematsverdriet, H. Fredriksson, J. Catal. 357 (2018) 176–1587.

[15] J. Ding, L. Li, H. Zhen, Y. Zuo, X. Wang, H. Li, S. Chen, D. Zhang, X. Xu, G. Li, Appl. Mater. Interfaces 11 (2019) 6042–6053.

[16] Y. Yigit, A. Genest, S. Terloev, J. Möller, G. Rupprechter, J. Phys. Cond. Matter 34 (2022) 354001.

[17] C. Hudy, F. Grybos, K. Steenbakkers, F. Gora-Marek, F. Zasada, Z. Sojka, Catal. Sci. Technol. 12 (2022) 5723–5741.

[18] J. Yu, Y. Yang, M. Zhang, B. Song, Y. Han, S. Wang, Z. Ren, L. Wang, P. Yin, L. Zheng, X. Zhang, M. Wei, ACS Catal. 14 (2024) 1281–1291.

[19] L. Gueci, F. Ferrante, A. Prestianni, F. Arena, D. Duca, Data in Brief 38 (2021) 107369.

[20] F. Arena, B. Gumina, A. Lombardo, C. Espro, A. Patti, L. Spadaro, L. Spiccia, Appl. Catal. B 162 (2015) 260–267.

[21] F. Arena, B. Gumina, C. Cannilla, L. Spadaro, A. Patti, L. Spiccia, Appl. Catal. B 170 (2015) 233–240.

[22] F. Arena, R. Di Chio, B. Fazio, C. Espro, L. Spiccia, A. Palella, L. Spadaro, Appl. Catal. B Environ. 210 (2017) 14–22.

[23] L. Gueci, F. Ferrante, A. Prestianni, R. Di Chio, A. F. Patti, D. Duca, F. Arena, Inorganica Chimica Acta 511 (2020) 119812.

[24] L. Gueci, F. Ferrante, A. Prestianni, F. Arena, D. Duca, Mol. Catal. 513 (2021) 111735.

[25] S. M. Lang, T. M. Bernhardt, J. M. Bakker, R. N. Barnett, U. Landman, J. Phys. Chem. A 125 (2021) 4435–4445.

[26] S. M. Lang, T. M. Bernhardt, J. M. Bakker, R. N. Barnett, U. Landman, Phys. Chem. Chem. Phys. 25 (2023) 32166–32172.

[27] T. Hayakawa, M. Arakawa, K. Minamikawa, S. Fujimoto, T. Kawano, A. Terasaki, Chem. Phys. Lett. 806 (2022) 140056.

[28] S. M. Lang, T. M. Bernhardt, J. M. Bakker, B. Yoon, U. Landman, Mol. Phys. 122 (2024) e2192306.

[29] S.-I. Naya, T. Kunimoto, H. Tada, Chem. Lett. 50 (2021) 1372–1374.

[30] Y. Zhao, D. G. Truhlar, J. Chem. Phys. 125 (2006) 194101.

[31] T. H. Dunning, J. Chem. Phys. 90 (1989) 1007–1023.

[32] M. Dolg, U. Wedig, H. Stoll, H. Preuss, J. Chem. Phys. 86 (1987) 866–872.

[33] M. J. Frisch, G. W. Trucks, H. B. Schlegel, G. E. Scuseria, M. A. Robb, J. R. Cheeseman, G. Scalmani, V. Barone, B. Mennucci, G. A. Petersson, H. Nakatsuji, M. Caricato, X. Li, H. P. Hratchian, A. F. Izmaylov, J. Bloino, G. Zheng, J. L. Sonnenberg, M. Hada, M. Ehara, K. Toyota, R. Fukuda, J. Hasegawa, M. Ishida, T. Nakajima, Y. Honda, O. Kitao, H. Nakai, T. Vreven, J. A. Montgomery, Jr., J. E. Peralta, F. Ogliaro, M. Bearpark, J. J. Heyd, E. Brothers, K. N. Kudin, V. N. Staroverov, R. Kobayashi, J. Normand, K. Raghavachari, A. Rendell, J. C. Burant, S. S. Iyengar, J. Tomasi, M. Cossi, N. Rega, J. M. Millam, M. Klene, J. E. Knox, J. B. Cross, V. Bakken, C. Adamo, J. Jaramillo, R. Gomperts, R. E. Stratmann, O. Yazyev, A. J. Austin, R. Cammi, C. Pomelli, J. W. Ochterski, R. L. Martin, K. Morokuma, V. G. Zakrzewski, G. A. Voth, P. Salvador, J. J. Dannenberg, S. Dapprich, A. D. Daniels, Ö. Farkas, J. B. Foresman, J. V. Ortiz, J. Cioslowski, D. J. Fox, Gaussian 09 Revision D.01, Gaussian Inc. Wallingford CT 2009.

[34] S. Grimme, Chem. Eur. J. 18 (2012) 9955.

[35] G. Luchini, J. V. Alegre-Requena, I. Funes-Ardoiz, R. S. Paton, F1000Research 9 (2020) 291.

[36] F. Arena, R. Di Chio, A. Palella, L. Spadaro, F. Frusteri, B. Fazio, S. Morandi, G. Martra, Appl. Catal. A Gen. (2021) 117917.

[37] F. Ferrante, C. Nania, D. Duca, Mol. Cat. 529 (2022) 112541.

[38] C. Nania, M. Bertini, L. Gueci, F. Ferrante, D. Duca, Phys. Chem. Chem. Phys. 25 (2023) 10460.

[39] L. Zhu, J. Wang, S. Rong, H. Wang, P. Zhang, Appl. Catal. B 211 (2017) 212–221.

[40] S. Wu, H. Liu, Z. Huang, H. Xu, W. Shen, Appl. Catal. B 312 (2022) 121387.

[41] H. Wang, H. Chen, Y. Wang, Y.-K. Lyu, Chem. Eng. J. 361 (2019) 1161–1172.

[42] F.-X. Tian, M. Zhu, X. Liu, W. Tu, Y.-F. Han, J. Catal. 401 (2021) 115–128.

[43] N. Jain, A. Roy, Mater. Res. Bull. 121 (2020) 110615.

[44] F. Arena, R. Di Chio, L. Filiciotto, G. Trunfio, C. Espro, A. Palella, A. Patti, L. Spadaro, Appl. Catal. B 218 (2017) 803–809.

[45] F. Arena, R. Di Chio, C. Espro, A. Palella, L. Spadaro, React. Chem. Eng. 3 (2018) 293–300.

[46] Y.-I. Hasegawa, R.-U. Maki, M. Samo, T. Miyake, Appl. Catal. A Gen. 371 (2009) 67–72.

[47] F.-X. Tian, H. Li, M. Zhu, W. Tu, D. Lin, Y.-F. han, Appl. Mater. Interfaces 14 (2022) 18525–18538.

[48] G. Li, Z. Zhao, W. Li, Z. Wei, X. Duan, Z. Zhang, J. Cheng, Z. Hao, Catal. Today 405-406 (2022) 337–347.

[49] J. Xu, Y.-Q. Deng, Y. Luo, W. Mao, X.-J. Yang, Y.-F. Han, J. Catal. 300 (2013) 225–234.

[50] W. Yang, Y. Z. snd F. You, L. Yan, Y. Ma, C. Lu, P. Gao, Q. Hao, W. Li, Appl. Catal. B 233 (2018) 184–193.

[51] K. Frey, V. Iablokov, G. Sáfrán, J. Osán, I. Sajó, R. Szukiewicz, S. Chenakin, N. Kruse, J. Catal. 287 (2012) 30–36.

[52] S. Liang, F. Teng, G. Bulgan, R. Zong, Y. Zhu, J. Phys. Chem. C 112 (2008) 5307–5315.

[53] J. Xu, T. Zhang, S. Fang, J. Li, Z. Wu, W. Wang, J. Zhu, E. Gao, S. Yao, Comm. Chem. 5 (2022) 97.

List of Figures

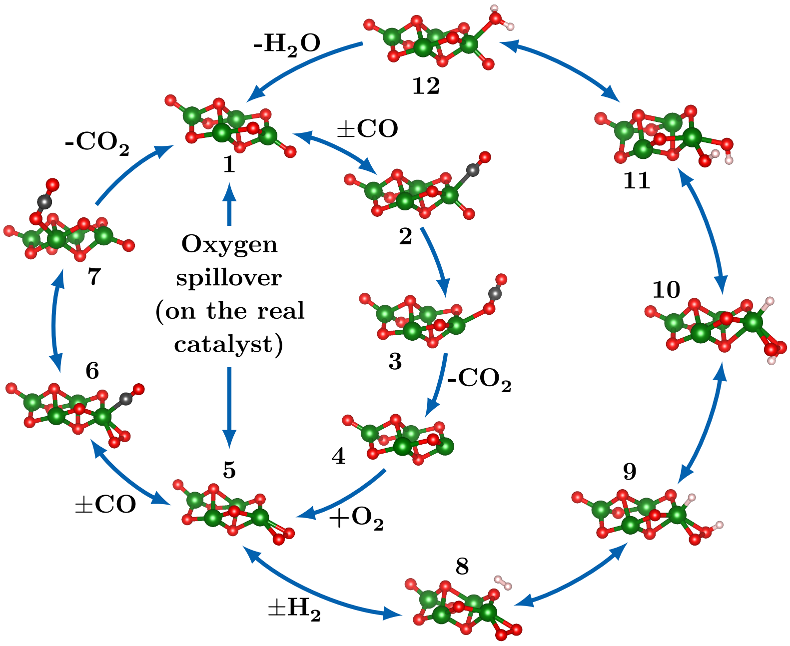

Figure 1: DFT-based mechanism for the oxidation of CO and H_2 on the Mn_4O_8 catalyst model. Mn: green, O: red, C: grey, H: pink.

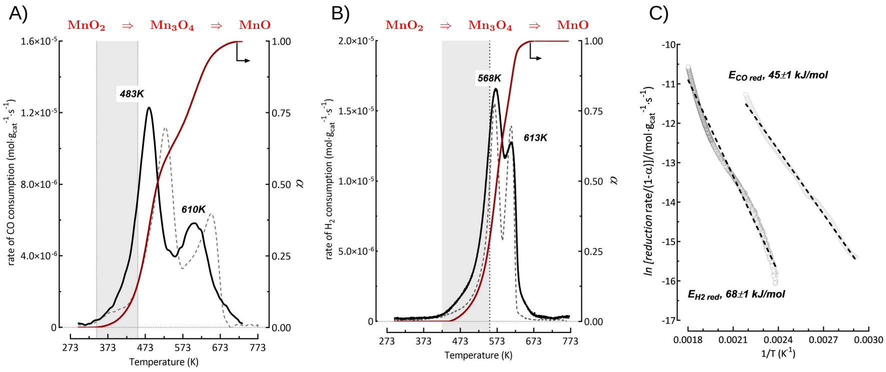

Figure 2: A) CO-TPR patterns and reduction degree (α, red curve) of the “as received” M5C1 catalyst (black solid curve) and MnO_2 sample (dashed curve) in the range of 293-773K; B) H_2-TPR patterns and reduction degree (α) of the “as received” M5C1 catalyst (black solid curve) and MnO_2 sample (dashed curve). C) Arrhenius plots of the reduction rates in the ranges of 343-453K (shaded area in A) and 423-568K (shaded area in B), respectively.

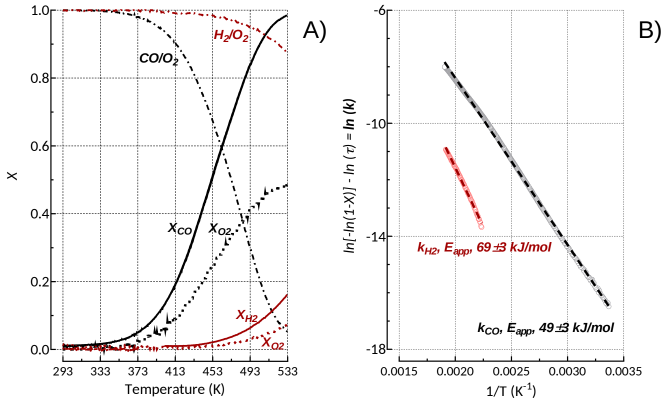

Figure 3: A) CO (black) and H_2 (red) oxidation activity of the M5C1 catalyst of in the range of 293-533K (p_{CO}, 1.0 kPa; p_{H_2}, 1.0 kPa; p_{O_2}, 1.0 kPa; GHSV, 180,000 h^{-1}); B) Arrhenius plot of CO (black) and H_2 (red) conversion data in the range of 353-523K elaborated by the integral 1^{st}-order kinetic model.

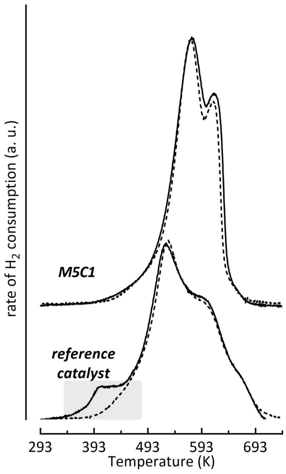

Figure 4: H_2-TPR patterns of “as received” (dotted lines) and “pretreated” (solid lines) M5C1 and reference $MnCeO_x$ (Mn_{at}/Ce_{at}, 1) catalysts. The pretreatment was carried out in situ at 673K in 5% O_2/He flow (30 min).

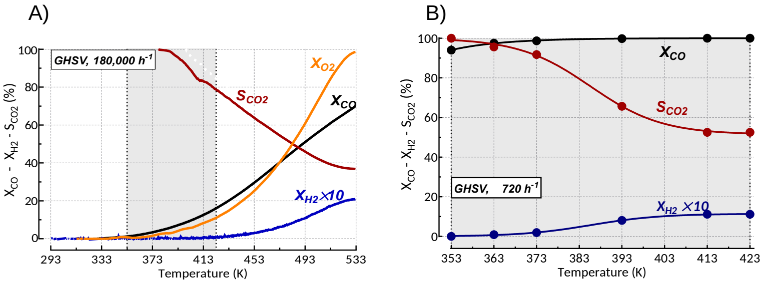

Figure 5: A) PROX data of the M5C1 catalyst under “differential conversion” conditions in the range of 293-533K (p_{CO}, 1 kPa; p_{O_2}, 1 kPa; p_{H_2}, 60 kPa; p_{He}, 38 kPa; GHSV, 180,000 h^{-1}); B) PROX data of the M5C1 catalyst under “integral conversion” conditions in the range of 353-423K (p_{CO}, 1 kPa; p_{O_2}, 1 kPa; p_{H_2}, 85 kPa; p_{N_2}, 13 kPa).

List of Tables

Table 1: Forward and backward Gibbs free energy barriers, ΔG, used for Christiansen analysis, calculated as a function of the temperature for each of the elementary steps of the CO and H_2 oxidation mechanisms reported in Figure 1.

Elementary process	**Free energy barriers ΔG/kJ mol^{-1} at T/K**							
	373		**423**		**473**		**523**	
1 + CO → 2	27.0[a]	0[b]	35.2	0	42.7	0	50.1	0
2 → 3	57.0	236.5	58.0	237.4	59.0	238.2	60.0	239.0
3 → 4 + CO_2	20.5	∞[b]	12.9	∞	5.3	∞	-2.3	∞
4 + O_2 → 5	0	∞	0	∞	0	∞	0	∞
5 + CO → 6	17.3	0	25.5	0	33.7	0	41.9	0
6 → 7	47.3	∞	48.0	∞	48.8	∞	49.6	∞
7 → 1 + CO_2	16.0	∞	8.4	∞	0.8	∞	-6.8	∞
1 → 5	0	∞	0	∞	0	∞	0	∞
5 + H_2 → 8	11.5	0	16.2	0	20.8	0	25.4	0
8 → 9	116.7	84.3	119.0	84.9	121.4	85.4	123.9	86.0
9 → 10	46.9	48.8	47.0	48.9	47.1	49.0	47.2	49.2
10 → 11	101.6	313.7	101.9	314.6	102.2	315.6	102.5	316.7
11 → 12	72.7	210.5	73.4	210.7	74.1	211.0	74.9	211.2
12 → 1 + H_2O	49.3	∞	41.9	∞	34.6	∞	27.3	∞

[a] In the SCM procedure, the values of ΔG associated to elementary steps where adsorption or desorption occurs were treated as free energy barriers.

[b] Very low (0) and very high (∞) values were used in the SCM procedure in order to completely allow or forbid, respectively, the corresponding elementary step.

Table 2: Reaction rates, s, at constant pressure for the CO and H_2 oxidation obtained by SCM at given temperature, T, values.

$\mathbf{s/s^{-1}}$	T/K			
	373	**423**	**473**	**523**
CO	1.47×10^{1}	3.61×10^{1}	7.41×10^{1}	1.36×10^{2}
$\mathbf{H_2}$	8.01×10^{-8}	3.14×10^{-6}	5.53×10^{-5}	5.77×10^{-4}

Table 3: Bulk and surface chemical properties of the M5C1 catalyst

Chemical composition (XRF)					**Surface chemical analysis (XPS)**				
[Mn]	[Ce] (wt %)	[K]	Mn/Ce	K/Mn (at/at)	Mn/Ce	K/Mn (at/at)	Mn(II)	Mn(III) (at %)	Mn(IV)
42.8	23.0	3.9	4.73	0.13	5.1	0.15	10.0	13.0	77.0

List of Scheme

	CO oxidation		**H_2 oxidation**	
(a)	$CO + \sigma O \rightleftarrows CO{-}\sigma O$		$2\,\sigma O \rightleftarrows \sigma + O_2{-}\sigma$	(a′)
(b)	$CO{-}\sigma O \rightleftarrows CO_2 + \sigma$		$\sigma + O_2 \rightleftarrows O_2{-}\sigma$	(b′)
(c)	$\sigma^{+}O_2 \rightleftarrows O_2{-}\sigma$	2×	$H_2 + O_2{-}\sigma \rightleftarrows H_2{-}O_2{-}\sigma$	(c′)
(d)	$CO + O_2{-}\sigma \rightleftarrows CO_2{-}O{-}\sigma$	2×	$H_2{-}O_2{-}\sigma \rightleftarrows H_2O{-}\sigma O$	(d′)
(e)	$CO_2{-}O{-}\sigma \rightleftarrows CO_2 + \sigma O$	2×	$H_2O{-}\sigma O \rightleftarrows H_2O + \sigma O$	(e′)
	$\mathbf{2\,CO + O_2 \longrightarrow 2\,CO_2}$		$\mathbf{2\,H_2 + O_2 \rightleftarrows 2\,H_2O}$	

Scheme 1: The proposed mechanisms for CO and H_2 oxidation reactions.